Electrochimica Acta 560 (2026) 148639

Contents lists available at ScienceDirect

Electrochimica Acta

journal homepage: www.journals.elsevier.com/electrochimica-acta

From RDE to Flowcell: The Impact of Iron on Nickel Catalyst Stability and Performance in Anion Exchange Membrane Water Electrolyzers

Ellis J. Donker [a,b,c,*], Marcelle Potgieter [a,d], Jordi Creus [a], Marco B.S. Wonink [a], Matheus T. de Groot [b,c], Roelof J. Kriek [d], Frode Seland [e], Svein Sunde [e]

[a] TNO, Westerduinweg 3, 1755 LE Petten, the Netherlands
[b] Department of Chemical Engineering and Chemistry, Sustainable Process Engineering Group, Eindhoven University of Technology, P.O. Box 513, Eindhoven 5600, MB, the Netherlands
[c] Eindhoven Institute for Renewable Energy Systems, Eindhoven University of Technology, PO Box 513, Eindhoven 5600, MB, the Netherlands
[d] Electrochemistry for Energy & Environment Group, North-West University, Private Bag X6001, Potchefstroom 2520, South Africa
[e] Department of Materials Science and Engineering, Norwegian University of Science and Technology (NTNU), NO-7491 Trondheim, Norway

ARTICLE INFO

Keywords:
Anion exchange membrane water electrolysis
Operando Raman spectroscopy
Degradation
Iron Incorporation
Nickel-based catalysts

ABSTRACT

Understanding how iron (Fe) influences nickel-based (Ni) catalysts in anion exchange membrane water electrolyzers (AEMWE) under industrial operational conditions is essential for enabling predictable and reproducible performance enhancement, yet the role of Fe in AEM flowcell conditions remains unexplored. This study investigates how Fe enhances Ni catalyst performance when it is intentionally incorporated into co-sputtered catalyst layers versus dissolved in the electrolyte. Preliminary rotating disk electrode experiments show that Ni-only catalyst layers initially display lower activity compared to NiFe catalysts although cycling can induce performance gains by Fe uptake towards comparable activity levels. In-situ Raman spectroscopy indicates that bulk NiOOH emerges only at low sputtered Fe contents but is suppressed above 23 wt% Fe, suggesting bulk NiOOH is not required to achieve the high activity observed for co-sputtered NiFe films. In flowcell experiments Fe-free Ni initially displays a high performance but degrades rapidly, while NiFe layers maintain stable performance over 100 h. In contrast to the RDE tests, Fe-spiked Ni samples show a gradual decrease in performance, partially attributed to Fe depositing in the reservoir and on the cathode as observed by SEM-EDX. For the pure Ni films, it is hypothesized that deviations from linear Tafel behavior at higher current densities are a consequence of diminishing availability of Fe. These findings help to understand Fe's role in enhancing Ni electrode performance as well as the need to account for Fe deposition phenomena, while showcasing the limitations of RDE testing for predicting real-world electrolyzer behavior.

1. Introduction

Anion exchange membrane (AEM) water electrolyzers (AEMWE) represent a promising technology in the field of hydrogen production through water electrolysis. The two half-cell reactions involved in a water electrolyzer include the hydrogen evolution reaction (HER) at the cathode and the kinetically sluggish oxygen evolution reaction (OER [1]) at the anode. AEM electrolyzers use an anion exchange membrane, which conducts hydroxide ions (OH^-), unlike their proton exchange membrane (PEM) counterparts that transport protons (H^+). This fundamental difference allows for AEMWE to operate in alkaline environments using earth-abundant Ni, Fe, B, and Co-based catalysts [2–4], mitigating the use of noble metal catalysts such as iridium and platinum that are required for PEMELs due to the acidic environment [5–7]. Additionally, by employing an AEM as an electrolyte AEMWEs can operate under differential pressure, unlike alkaline electrolyzers (AWE). Although promising, the performance and stability of AEM electrolyzers do call for improvements to be competitive with PEMEL, especially regarding the lifetime and the efficiency of PGM-free catalytic coatings for the kinetically sluggish OER [2,4].

It has been known for many years that the presence of iron (Fe) can significantly boost the activity of nickel (Ni) electrodes in alkaline environments [8], both for the OER [9,10] and the HER [9]. Corrigan showed that co-deposited Fe as low as 0.01% lowered OER

* Corresponding author at: Westerduinweg 3, 1755 LE Petten, the Netherlands.
E-mail address: ellis.donker@tno.nl (E.J. Donker).

https://doi.org/10.1016/j.electacta.2026.148639
Received 19 November 2025; Received in revised form 4 March 2026; Accepted 8 March 2026
Available online 9 March 2026

overpotentials, although an even more drastic improvement was observed for Fe concentrations above 10 % with the formation of NiFe hydrous oxide reaching overpotential values of ~200 – 250 mV at 10 mA cm^{-2}. Both in the electrolyte and the bulk catalyst layer, the presence of Fe can alter the electrochemical properties, catalytic activity, and overall efficiency of the electrolyzer [11]. During recent years, many investigations have tried to elucidate the exact role Fe plays during OER electrocatalysis.

There are currently three hypothesized mechanisms for the OER and the role Fe has in it [12,13]. The first is the conventional 4-electron transfer OER with 4 proton-coupled electron transfer steps [14], where the rate-determining step is the O-O coupling via OH^- attack on Fe=*O*, also called a mono-nuclear mechanism since it takes place on a single active site, which is currently believed to be Fe [12,15]. The mono-nuclear mechanism was found experimentally for NiFe layered double hydroxides (NiFe-LDH) structures specifically, where the lattice O of NiOOH is exchanged with the O from OH^- [14,16,17]. In the bi-nuclear mechanism two water molecules are oxidized to =*O* at two adjacent sites, which then chemically form an O-O bond [12,18]. The third mechanism is the bifunctional mechanism, which was initially only identified using density functional theory calculations [19–21], but has been proven to exist for NiOOH/FeOOH catalysts experimentally [14]. Here Fe=*O* acts as the oxygen evolving site, while Ni^{III}-O serves as hydrogen atom acceptor [20,22]. It is hypothesized that the proton transfer from the Fe^{3+}-ion is sluggish, creating a kinetic barrier for higher Fe values in NiFe, shifting the $Ni(OH)_2$ to NiOOH redox peak to higher potentials at higher Fe content, something that has been observed in several studies [23,24]. These studies show proof of two different mechanisms where the role of Fe in the OER is different, but it is not proven that these are the only two exclusive possibilities.

Fe has been found to replace part of the Ni in the bulk $Ni(OH)_2$ structure, which results in a NiFe-LDH structure and is a popular theory on how the OER benefits from Fe [25]. Additionally, several studies have suggested that the surface Fe plays a larger role in the OER activity, and that the OER takes place close to the surface [25–29]. In a recent publication, Heath *et al.* have studied the impact of the Ni oxidation state on Fe incorporation. They evaluated Ni, NiO, and NiNiO sputtered thin films in solutions with various Fe contents and confirmed that the surface Fe, rather than the electrolyte Fe, enhances the activity towards the OER. While different Ni oxidation states led to the same activity, more Fe was incorporated in the surface of NiNiO than that of Ni and NiO [28]. According to the Bode model [30], when a positive potential is applied Ni initially forms α-$Ni(OH)_2$, followed by γ-NiOOH. Through electrochemical ageing, α-$Ni(OH)_2$ transforms to β-$Ni(OH)_2$, which can then be further oxidized to β-NiOOH and is more active towards OER [30–36]. β-NiOOH can further oxidize to the more open γ-NiOOH structure, the generally agreed less active phase [37–40], which can be prevented by incorporation of Fe [41].

Although there are publications on the influence of dissolved Fe in the electrolyte in AELs [42], such a study has not been performed yet on AEMWEs. To the best of our knowledge, a study that compares Fe deposition on the anode to Fe spiking in the electrolyte does not exist yet.

This study aims to identify whether the known improvement in Ni catalysts from Fe addition is more pronounced and sustainable when it is part of the catalyst formulation, versus when Fe is dissolved in the electrolyte in an AEMWE. The secondary goal of this study is to assess whether the role of Fe as studied in the rotating disk electrode (RDE) configurations is in line with the role of Fe in an AEMWE flow cell. To achieve this, the study involved comprehensive testing and analysis consisting of RDE testing, as well as in-situ Raman spectroscopy to get a better understanding of the active site. Afterwards, anodes with and without Fe in the catalyst layer and electrolyte were assessed for 100 h in a single-cell AEM electrolyzer at 1 A cm^{-2}.

2. Experimental

2.1. Sputtering

The RDE glassy carbon (GC) electrodes and the 600 μm stainless steel (SS) felt anodes for the flow cell tests were sputtered under ultra-high vacuum conditions, employing a plasma vapor deposition (PVD) system (PVD products, USA). Prior to catalyst deposition, the 0.196 cm^2 GC disks electrode inserts (Gigradur G, HTW Germany) were polished in a figure of eight movement on a microfiber cloth using 0.1 μm diamond paste, rinsing with ultrapure water, followed by polishing using a 0.05 μm aluminum suspension (Gamma Micropolish II, Beuhler). Afterwards, they were rinsed and consecutively sonicated for 15 min in each of the following solvents: toluene (Merck), ethanol (Merck), ultrapure water, and isopropanol (Merck). The films containing Ni were sputtered using Direct Current (DC) magnetron sputtering. Pure Ni and Fe targets were used (both 99.99 % from ACL Alloys, Inc.) After setting the system to the base pressure of 10^{-7} Torr, calibration of the Ni target was carried out with 25 mL/min Ar flow and a chamber pressure of 10 mTorr, which resulted in the following calibration equation: $y = 0.1297x - 0.3549$, with y being the sputtering rate (nm/min) and x the power (W). Different percentages in Fe were obtained by altering the power, as is shown in Table 1, whereas the Ni sputtering power was kept at 90 W. Subsequent to sputtering, the composition of the layer was validated using SEM-EDX, of which an example can be found in Figure S3. Table 1 shows that the percentages of Ni and Fe for the RDE working electrode deviate slightly between what was calculated and what was determined with SEM-EDX. What was calculated to be 3.47% was found to be 0.11% lower; 23.51 was 1% lower; and 43.75 was 4% higher. In the paper the calculated mol% will be used.

2.2. RDE testing

Electrochemical characterization was performed in a rotating disk electrode experimental setup (Pine Research Instrumentation) by employing a Bio-Logic SP150 potentiostat, using a Julabo F12-ED chiller and a water jacketed cell to maintain a constant temperature of 25 °C. As electrolyte, 0.1 M KOH (Sigma Aldrich, semiconductor grade 99.99 %) was used with 5 different Fe contents: purified (2.8 ppb, method according to Trotochaud et al. [24]), unpurified (4.9 ppb Fe), and addition of 0.02 mM Fe, 0.1 mM Fe, and 0.2 mM Fe. This was done by spiking Fe (III) nitrate nonahydrate ($Fe(NO_3)_3 \cdot 9\ H_2O$, 99.9999 % trace metal basis, Sigma Aldrich). As counter electrode (CE) and reference electrode (RE) a Pt-wire (ALS-Japan) and a Hg/HgO electrode (ALS RE-61AP) were used, respectively. All electrochemical tests were performed at a rotation rate of 1600 rpm. Prior to each cyclic voltammogram (CV) experiment N_2 was bubbled through the electrolyte for 20 min. Cyclic Voltammograms (CVs) were recorded within the potential range of 0.3 – 0.6 V vs. Hg/HgO employing a scan rate of 20 mV s^{-1}. Linear sweep voltammetry (LSV) was performed before and after potential cycling at 5 mV s^{-1} in the potential range of 0 – 0.6 V vs Hg/HgO. The offset potential was obtained from the average of the voltage intercept of the x-axis by conducting cyclic voltammetry at 10 mV s^{-1} employing a

Table 1
Settings and resulting properties for sputtering Ni and NiFe samples for RDE disks and flowcell PTLs.

Sample	Ni DC power (W)	Fe DC power (W)	Thickness (nm)	Time (min, s)	Fe calculated (mol %)	Fe from SEM-EDX (mol %)
1	90	90	51.2	3, 0	43.75	47.77
2	90	50	40.4	3, 36	23.51	22.5
3	90	10	50.7	4, 15	3.47	3.28
4	90	-	50	4, 2	0.00	0.00

coated GC disk as working electrode and a Pt wire CE within the hydrogen oxidation/reduction potential range -1.0 – 0.9 V vs. Hg/HgO. All measured potentials were converted to potentials relative to the reversible hydrogen electrode (RHE) by subtracting the offset potential. To obtain the overpotentials, the standard potential of the OER, 1.23 V, was subtracted from the potentials from LSV curves. The measurements were conducted with 100 % iR compensation in EC-Lab, as measured at OCV using 100 kHz and 20 mV amplitude.

2.3. Flow cell testing

The performance of the sputtered anodes was evaluated in a stainless steel 5 cm^2 AEM Water Electrolyzer from Dioxide Materials™ with a single serpentine flowfield assembled using a torque of 2 Nm. The cathode and membrane used in the flow cell tests were the H_2O cathode from Dioxide Materials™ and an Aemion+™ reinforced membrane from Ionomr Innovations Inc., respectively. The H_2O cathode contains 2 mg cm^{-2} Raney Ni and 5 mol % LIQIion™ Nafion™ binder on 300 μm Ni fiber paper. The membrane was always soaked in 1 M KOH for 24 h prior to cell assembly to exchange the functional groups to their OH^- form. Experiments were executed with 1 M KOH electrolyte (Sigma Aldrich KOH pellets >85 % purity). On the anode side two 300 μm Teflon gaskets were used, on the cathode side one 300 μm Teflon gasket, matching the thickness of the electrodes. The test sequence is shown in Figure S1.

The tests were performed employing an in-house designed test bench. The potentiostat used was a VMP-300 (Biologic), which employed 2 booster modules (max 5 V and 20 A). Two peristaltic MasterFlex Easy-Load II pumps were used to circulate the anolyte and catholyte, using flexible tubing (Puri-flex L/S 16). In the rest of the setup PFA tubing was used: 3/8th inch diameter, and ¼ inch diameter for the last few centimeters leading to the cell to match the connection diameter. The cell temperature was maintained at 60 °C using a 50 W, 110 V Dioxide Materials™ cell heater designed for their 5 cm^2 cells. This was controlled using a temperature regulator FR100 by CasCade Automation Systems B.V., connected to two thermocouples, of which one was taped to the top of the anode flowfield, and one to the top of the cathode flowfield to regulate both sides separately. The electrolyte temperature of the inlets and outlets was also monitored by four thermocouples. The anolyte and catholyte reservoirs were connected at the bottom through a 7 cm 3/8th inch diameter tubing to allow diffusion of hydroxide ions between the reservoirs. Nitrogen gas was purged through these two reservoirs 10 min prior to the experiment, and 10 min into the start of the experiment. For all tests anolyte and catholyte samples were collected after its preparation (fresh electrolyte) and at the end of the test for ICP-MS measurements.

2.4. Characterization

2.4.1. Impedance data

Impedance data was fitted with equivalent circuit model (ECM) fitting. The equivalent circuit consisted of an inductor, a series resistance, and one or two constant phase elements, depending on the number of peaks identified by the distribution of relaxation times (DRT) model (LR(QR)(QR) or LR(QR)). The DRT model that was used is equal to the one described by Ranz et al. [43], with parameters $\lambda = 10^{-2}$ and $m = 100$.

2.4.2. In-situ Raman

In-situ Raman Spectroscopy was performed in the setup as described by Faid et al. [44]. Using a laser with 500 mW power and $\lambda = 532$ nm, the probing depth δ [m] can be calculated from the inverse of the adsorption coefficient α [m^{-1}]. $\delta = \frac{1}{\alpha}$, with $\alpha = \frac{4\pi\kappa}{\lambda}$, where κ [-] is the extinction coefficient, which is 3.4946 for Ni and 2.8954 for Fe at 532 nm [45]. Therefore, the probing depth of the Raman is 12.1 – 14.6 nm for combined NiFe catalysts.

2.4.3. ICP-MS

Inductively coupled plasma mass spectrometry (ICP-MS) was used to determine the concentration of iron, cobalt, molybdenum, magnesium, chromium, and aluminum. Prior to analysis the samples were diluted 20 times in the following manner: 0.25 mL sample, 0.25 mL 1 M HNO_3, 5 mL 0.1 M HNO_3 with trace HF. An Agilent 7700x ICP-MS system was used for this, consisting of ICP-MS, autosampler, vacuum pump, cooling, and Agilent MassHunter software.

2.4.4. SEM-EDX

To determine the physical appearance and composition of the sputtered flowcell samples semi-quantitatively, scanning electron microscopy (SEM, FEI Quata FEG 250) with an integrated XMax 20 energy dispersive x-ray (EDX) system (Oxford instruments) was employed. SEM-EDX imaging of the electrodes before and after electrolysis were also taken, on a Hitachi FE-SEM SU-70.

3. Results and discussion

3.1. Electrocatalytic activity in RDE

RDE findings of co-sputtered NiFe (Fe contents of 0, 3, 23, 47 mol %) reveal that the OER overpotential at 10 mA cm^{-2} is 150–200 mV lower for both sputtered NiFe and Ni with Fe in the electrolyte (purified, 0.02, 0.1, 0.2 mM) compared to the ~500 mV overpotential for sputtered Ni in the purified electrolyte (Fig. 1a). For none of the electrodes there is a noticeable benefit of increasing the Fe concentration in the electrolyte beyond 0.1 mM. These results show that Fe within the electrolyte solution enhances the OER activity to the same extent as Fe within the catalyst layer, and that there is a maximum reduction in overpotential due to Fe addition, as it does not keep decreasing with increasing Fe content.

Fig. 1b shows the CVs that were recorded with different Fe percentages in the catalyst layer. Characteristic redox peaks for CVs of Ni in alkaline media include the transformation between Ni^{II} and Ni^{III} according to Reaction 1 $Ni(OH)_2 + OH^- \leftrightarrow NiOOH + H_2O + 4e^-$ [1]. For Ni electrodes with Fe in the bulk or in solution, Görlin *et al.* has shown that the Ni^{II} to Ni^{III} peak shifts to the right and becomes smaller with increasing Fe content [22]. The decrease of the size of the peak can partially be attributed to the Fe content that leads to a lower mol % of Ni in the catalyst layer. Additionally, the shift to higher potentials can be ascribed to the formation of the reactive $Ni^{2+}Fe^{3+}(OH)(O)^{\delta-}$ during OER, which is followed by the transfer of a proton and electron from the Ni site. Görlin *et al.* described the first proton transfer step from the Fe^{3+} site as slow, creating a kinetic barrier for higher Fe content and shifting the Ni redox peak to higher potentials for higher Fe content [22].

Fig. 2 shows cyclic voltammograms of cycles 1 and 30 for pure sputtered Ni, Ni co-sputtered with 47 mol % Fe in purified KOH, and pure Ni with 0.2 mM Fe. For the catalyst layer with only Ni, it is evident that cycling in 0.2 mM Fe containing electrolyte shows good activity from the start, but it is further improved by cycling. On the other hand, for Ni in purified KOH cycle 1 shows limited activity towards OER, but this increases with cycling. Since Trotochaud *et al.* have shown that Ni itself is not extremely active towards OER [24], this activity must be caused by the remaining 2.8 ppb Fe that remained after purification [24, 46]. However, when 47 mol % Fe is present in the catalyst layer, the OER activity is high from the first cycle, before formation of NiOOH in the bulk can take place. Moreover, when Fe is present in the catalyst layer, cycling has no additional benefit for the performance, as is evident from the OER peak from the 30th cycle that can hardly be distinguished from the first cycle. This finding is interesting, as it has often been suggested that the NiOOH matrix serves as a conductive medium with Fe as the active site in this structure [20,26,47,48]. While these findings confirm that Fe plays a crucial role in the OER, they show that bulk NiOOH is not required for good activity when Fe is readily present in the bulk. This

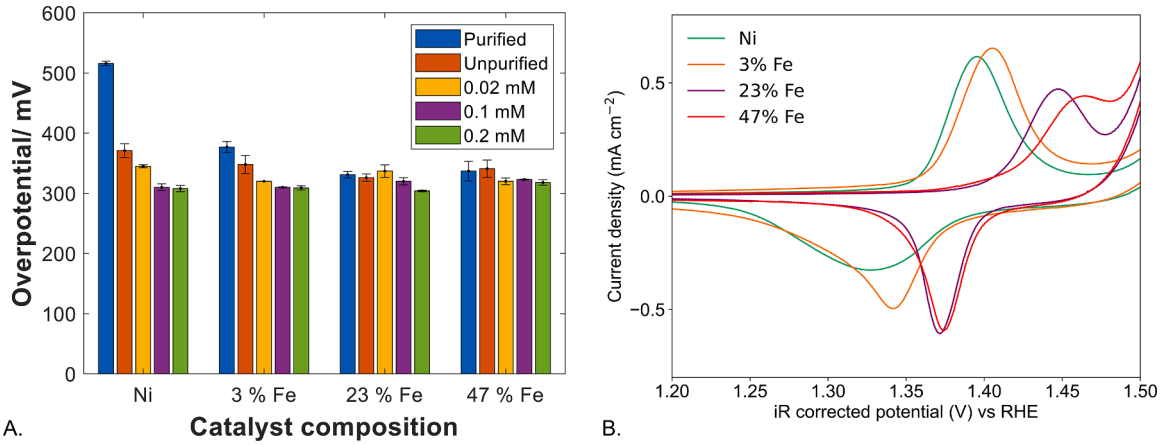

Fig. 1. RDE experiments performed at 1600 rpm, at 25 °C in 0.1 M KOH using Pt wire as CE, Hg/HgO as reference electrode, and glassy carbon disk as working electrode. 100 % iR corrected during measurement. a. Overpotentials at 10 mA cm^{-2} after stabilization, 30th cycle for various catalyst compositions (x-axis) and Fe concentrations in solution (legend); b. cyclic voltammogram for different sputtered Fe contents in purified solution, as measured by RDE.

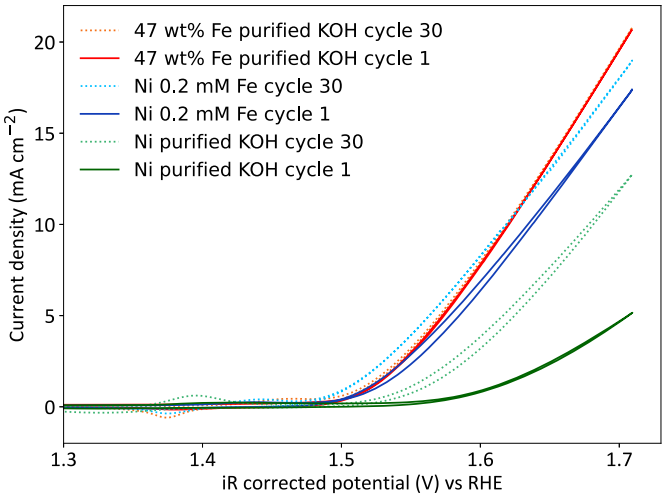

Fig. 2. Influence of Fe content in the catalyst layer and electrolyte on OER activity in CVs, 100 % iR corrected. RDE experiments performed at 1600 rpm, at 25 °C in 0.1 M KOH using Pt wire as CE, Hg/HgO as reference electrode, and sputtered glassy carbon disks as working electrode. The three different samples are 1. sputtered Ni in purified KOH (green), 2. Sputtered Ni in KOH with 0.2 mM Fe in electrolyte (blue), 3. Sputtered NiFe (47 mol % Fe) in purified KOH (red). Cycles 1 (full; red, dark blue, dark-green) and cycles 30 (dotted; orange, light-blue, light-green).

does not mean that the popular NiOOH theory does not hold true for a Ni catalyst with Fe in the electrolyte, as that has not been investigated in this study. The findings are in line with what has been shown by Burke *et al.* and Friebel *et al.*, and that the optimal adsorption energies for OER intermediates are at Fe sites, not Ni or Co sites [47,49].

Additionally, these findings do not entirely align with the study of Farhat *et al.*, who suggested that OER activity of NiFe-Oxo/Hydroxide films are not sustainable without Fe in solution, as they saw a continuous loss in performance already after the first CV [25], which we do not observe; after thirty cycles the activity towards OER remains the same without additional Fe in the solution, indicating that this type of catalyst layer actually shows good stability, which will also be shown in the flowcell tests. However, this discrepancy may be explained by the differences in deposition method affecting Fe incorporation.

To evaluate the hypothesis that a NiOOH structure is not needed to obtain good activity with Fe in the bulk of the electrocatalyst, operando Raman spectroscopy measurements were performed on the four catalyst layers in purified KOH (Fig. 3). The probing depth is 12–14 nm as discussed in the section "In-situ Raman" in the Methods section. The broad peak beyond 3000 cm^{-1} corresponds to water [1], and the peaks at 1355 and 1580 cm^{-1} to glassy carbon [50]. Peaks corresponding to γ- and β-NiOOH can clearly be distinguished at 460 and 550 cm^{-1} [1,37,51,52] above 1.45 V for catalyst layers with 0 and 3 mol % Fe. At 1.45 V vs RHE, Ni^{II} is oxidized to Ni^{III}, as $Ni(OH)_2$ is oxidized to NiOOH. Surprisingly, these peaks do not appear when 23 or 47 mol % Fe is present in the catalyst layer, showing that under these experimental conditions bulk NiOOH is not detected for catalyst layers with Fe. We do, however, expect formation of NiOOH on the surface even with higher Fe contents, since there is still a small redox peak visible where Ni^{II} oxidizes to Ni^{III}, though in such low amounts that it is not detectable with Raman. Alternatively, due to the shift to higher potentials as discussed for Fig. 1, the formation of NiOOH might be taking place at higher potentials than where OER is taking place and Raman peaks cannot be measured due to bubble formation.

3.2. Flow cell tests

The RDE results showed that the activity of Ni towards the OER is boosted by the presence of Fe, independent of being added to the catalyst layer or to the electrolyte. They also showed that NiFe catalysts are active from the start, whereas Ni catalysts require cycling to improve activity. Unlike the ideal conditions at a RDE, the interplay between the different components should be studied in a flow cell: the porous transport layers, catalyst layers, and membrane. Only then it can be established whether the addition of Fe to the catalyst layer or to the electrolyte is a sustainable and durable solution to improve OER performance under relevant operating conditions in a flowcell. It should be mentioned that while 0.1 M KOH was used for the RDE tests, 1 M KOH was used in the flowcell. It has been shown that having a higher molarity in 3-electrode setups can shift the Ni oxidation peak and OER offset cathodically [53] and cause faster transition of α-NiOOH to γ-NiOOH [54,55]. Although the speed of transitions and location of peaks might have slightly varied, the relative trends in the RDE data that are used to compare to the flowcell would have been the same at 1 M KOH [56,57], specifically with respect to the influence of Fe [53].

The electrochemical results are discussed for sputtered Ni and NiFe (23 mol %) on 600 μm SS in (unpurified) 1 M KOH with or without 0.2 mM Fe. For each test, an Aemion+™ membrane and Dioxide Materials™ Raney Ni cathode were used and tested in a stainless steel 5 cm^2 Dioxide Materials™ cell. Tests started with a stabilization period of 16 hours at 2 V, followed by the beginning of life (BoL) that consists of impedance measurements at various current densities and a polarization curve. Afterwards, the durability of the samples was evaluated for 100 hours at

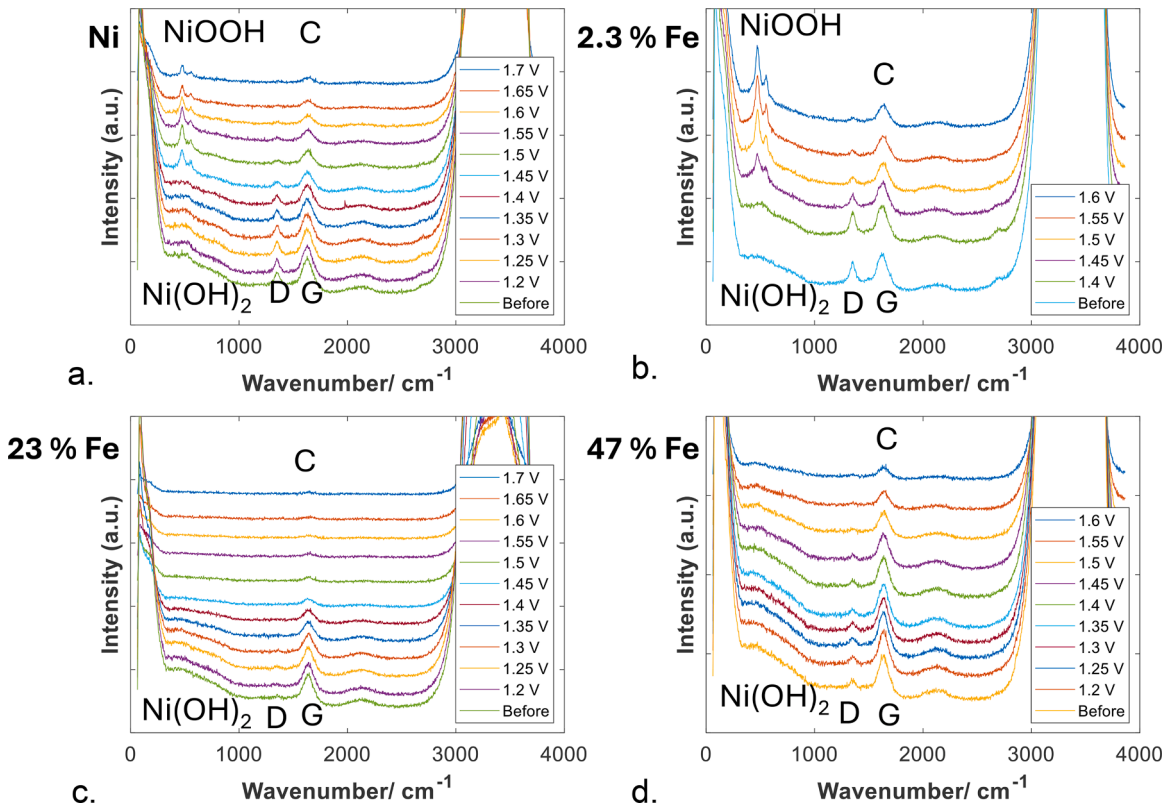

Fig. 3. In-situ Raman spectroscopy during RDE measurements for various sputtered Fe contents in purified KOH. At 1355 and 1580 cm^{-1} the D-band and G-band of carbon (C) can be seen, respectively, originating from the GC disk working electrode. Above 3000 cm^{-1} the broad band of water (originating from the electrolyte), and at 460 and 550 cm^{-1} the bonds that represent NiOOH.

1 A cm^{-2}, after which the end of test (EoT) was measured, using the same protocol as the BoL.

The difference between the ideal environment at the RDE tests and industrially relevant flow cell tests can already be distinguished in the first few hours of the stability tests shown in Fig. 4. Ni with and without 0.2 mM Fe in the electrolyte start off at the same potential of 2.11 V, while in RDE Fe-free Ni at the first cycle did not even reach half the activity of Ni with 0.2 mM Fe. This indicates that for a short-term measurement, the Fe that is introduced from impurities in the KOH pellets (1–15 μM) is sufficient to shortly boost the performance. Both these samples lose performance, although over a vastly different time range: the test without added Fe in the electrolyte reaches the set voltage limit of 2.2 V after 18 hours, while Ni with 0.2 mM Fe stabilized at 2.16 V in the last 24 hours of the 100-hour test. On the other hand, when Fe is present in the catalyst layer, the initial activity is not boosted as much as was expected from the RDE tests: within the first minutes the voltage increases from 2.12 to 2.15 V and remains stable at this voltage for 100 hours. The exact reason for this lack of activity during the stability test remains unclear and is even more surprising since the NiFe sample reached the highest current density during the 16-hour conditioning of the samples (Figure S6). It should be mentioned that the NiFe catalyst was not optimized, leaving room for optimizing this layer. For example, a treatment can be done to increase the surface roughness and thus area, making use of nanofibers as a substrate [58], or the composition of the layer can be improved by incorporating oxygen atoms in the layer [28].

The difference between these three anodes indicates that both Fe in the catalyst layer and the electrolyte suppresses the degradation rate compared to the sputtered Ni anode without added Fe, where the overvoltage increases quickly. Even though the initial performance of the sputtered Ni with added Fe is higher than the NiFe sample it degrades faster and reaches the same potential after 100 h. This can partially be attributed to the Fe sink due to precipitation as red $Fe(OH)_3$ due to the low solubility of Fe in a high pH solution [59] and to the reduction of Fe^{3+} to metallic Fe on the cathode [60,42,61], which will

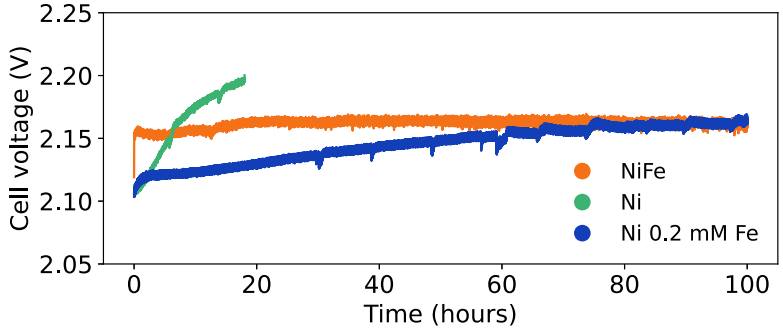

Fig. 4. 100 h stability test at 1 A cm^{-2} at 60 °C using 1 M KOH in 5 cm^2 flowcell of Ni or NiFe sputtered anodes, with or without 0.2 mM Fe in the electrolyte, with Dioxide Materials™ cathode and Aemion+ membrane.

take longer for solutions with a higher Fe content, but eventually lead to the same result.

To further understand the observed behavior, we analyzed the polarization curves and impedance curves recorded during BoL and EoT at 3 current densities for all 3 tests. In Fig. 5 the BoL and EoT polarization curves are shown, both normal (a) and as iR-corrected Tafel plots (b). The uncorrected polarization curves do not reveal clear trends, besides the improvement in performance after 100 hours for the Ni samples, a regeneration phenomenon of Ni electrodes when Fe is present as an impurity that has been studied by Poli et al. (2025) [62]. The main difference between them is revealed in the Tafel plots (Fig. 5b), where at higher current densities the slope of the Ni sample without spiked Fe shows a strong curvature towards higher potentials, both during BoL and EoT. The curvature is also connected to their stability: samples that are more stable in the durability test show a straighter line in the Tafel plot. This change in the Tafel slope at higher current densities for low Fe concentrations using Ni electrodes has also been observed already in the 1980s by Corrigan *et al.* [8]. Similarly, Watson *et al.* have also observed such behavior, although they did not vary the Fe content. They attribute this change to migration and diffusion effects [63,64]. Since the only variable in these tests was Fe, we speculate that at higher current densities there are a limited number of Fe sites for the reaction (vide infra).

To further explain the observed behavior in the durability tests we conducted EIS measurements to differentiate between kinetic and ohmic contributions in the cell. Fig. 6a shows the Nyquist plots of the 3 samples at 0.2 A cm^{-2} at BoL, and the EoT plots (Figure S9). Analysis by Distribution of Relaxation Times (DRT) of the data confirms that the Nyquist plots consist of two semicircles. ECM fitting shows they have varying ohmic resistances, charge transfer resistances, and capacitances. Firstly, the boxplots (Fig. 6b) show that during BoL Ni with 0.2 mM Fe has the highest ohmic resistance at 162 $\pm$ 2 mΩcm^2, followed by NiFe (134 $\pm$ 1 mΩcm^2), and Ni (126 $\pm$ 2 mΩcm^2) being the lowest. The large ohmic resistance of Ni with 0.2 mM Fe is surprising: the presence of Fe in the electrolyte seems to have a negative effect on the series resistance. Friebel *et al.* have observed insulating FeOOH on the surface of their electrode for increased Fe concentrations on the anode [47]. Since, in our experimental setup, the dissolved Fe can reach the cathode, it is also plausible that the increased ohmic resistance is caused by the deposition of metallic Fe on the cathode [65–67]. Although multiple studies have found HER improvements from the addition of Fe to the electrolyte, which they attributed to increased surface area, their substrates did not contain a catalyst layer nor were adapted to obtain a high surface, thus, would benefit from the high surface area from the deposited Fe dendrites [42,67]. In SEM-EDX needle-like Fe deposits were observed on the fibers of the cathode PTL for the test of Ni with 0.2 mM Fe in the electrolyte (Figure S4), therefore, both these theories could hold true. Taking into account the steep increase of the Tafel slope after 100 h to 240 mV/dec (Fig. 5b), we speculate that the observed Fe layer on the cathode is reducing the HER kinetics by covering the Raney Ni catalyst. However, in our configuration, it is not possible to distinguish between anode and cathode in operando, so no conclusion can be drawn regarding the overpotentials of the anode and cathode individually. Lastly, as shown in Figures S6–9, the reproducibility of the NiFe samples varied during the first hours of the test, which could be another cause for the differences in ohmic resistances.

For all samples, the ohmic resistance decreased after 100 hours (Fig. 6b). In PEM electrolyzers this is often attributed to membrane thinning due to a Fenton reaction [68], and can be accelerated by the presence of Fe [69]. Peroxides degrade AEMs as well [70], however, according to our knowledge it has not been investigated whether they persist long enough in the high pH environment to do any damage. What stands out is the substantial decrease in ohmic resistance of 20 mΩ cm^2 for NiFe over 100 hours. Considering that the ohmic resistance was high at the start, it would seem that either the removal of an insulating layer on the electrode has taken place over time, or the membrane has thinned due to a Fenton reaction, or the ionomer and catalyst have reorganized [71].

The polarization resistance (R_p), the limit of the impedance at zero frequency [72], is obtained from ECM fitting of the impedance data at various current densities, of which two current densities are depicted in Fig. 7. As expected, at 0.2 A cm^{-2} (Fig. 7a), we observe that Ni without Fe has the largest polarization resistance, which is in line with the RDE experiments of this study, as increased Fe concentrations reduce the charge transfer resistance [28,73], the change in faradaic current in the double layer over the change in voltage, while the surface state is constant [72]. At 0.6 A cm^{-2} it is more pronounced that the polarization resistance is higher for Ni with respect to the samples that include Fe. The polarization resistance consists of the two charge transfer resistances, which directly relate to the Tafel slope (Fig. 5b) [74,75]. When we compare them, we observe that the larger the polarization resistance, the more strongly the Tafel slope curves up at higher current densities, which is the case for the tests with less Fe and more pronounced at higher current densities. This is in accordance with our previously mentioned hypothesis that the availability of Fe, required for the OER, has become limiting at higher current densities. This is in line with what was suggested by Friebel *et al.*, that Fe acts as the site for adsorption of

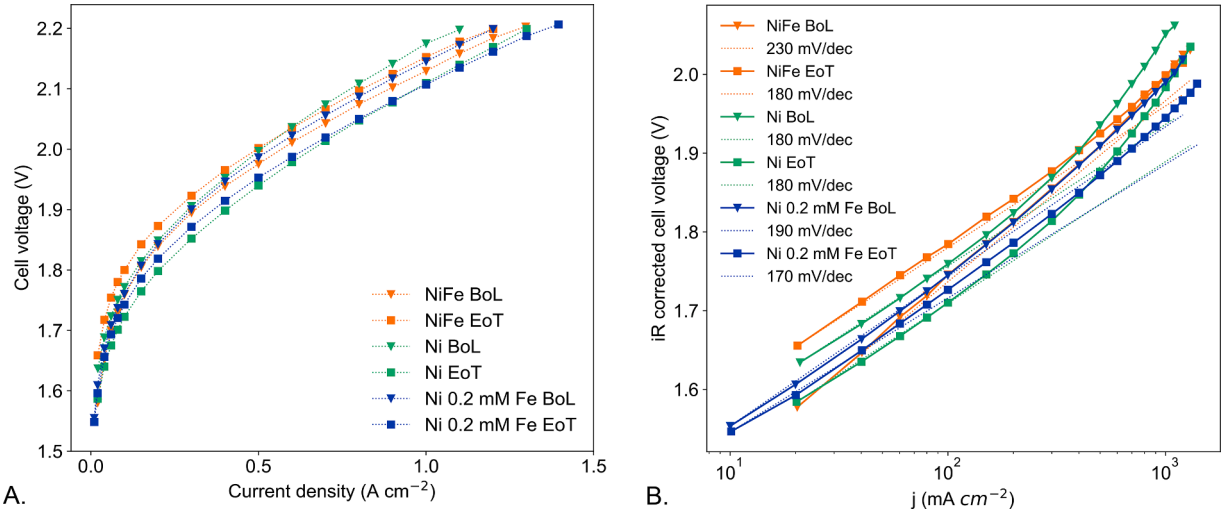

Fig. 5. BoL (triangles) and EoT (squares) polarization curves at 60 °C using 1 M KOH in 5 cm^2 flowcell of Ni (blue and green) or NiFe (orange) sputtered anodes, with (blue) or without (orange and green) 0.2 mM Fe in the electrolyte, with DIOXIDE MATERIALS™ cathode and Aemion+ membrane. a. Normal and b. iR corrected.

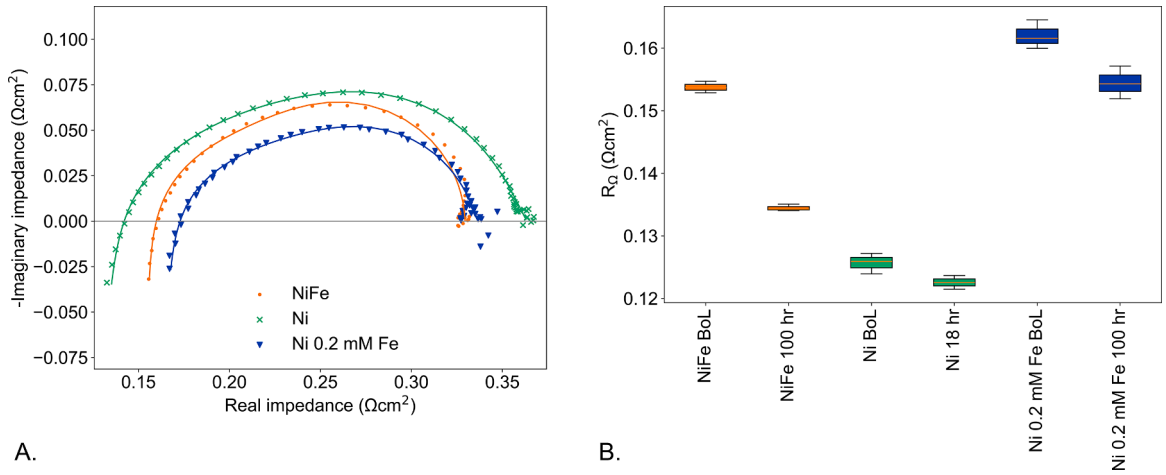

Fig. 6. EIS recordings at 60 °C using 1 M KOH in a 5 cm^2 flowcell with Ni or NiFe sputtered anodes, with or without 0.2 mM Fe in the electrolyte, with a DIOXIDE MATERIALS™ cathode and an Aemion+ membrane. (a) Nyquist plots collected during BoL at 0.6 A cm^{-2}. (b) Boxplots of ohmic resistances during BoL and EoT of all the samples.

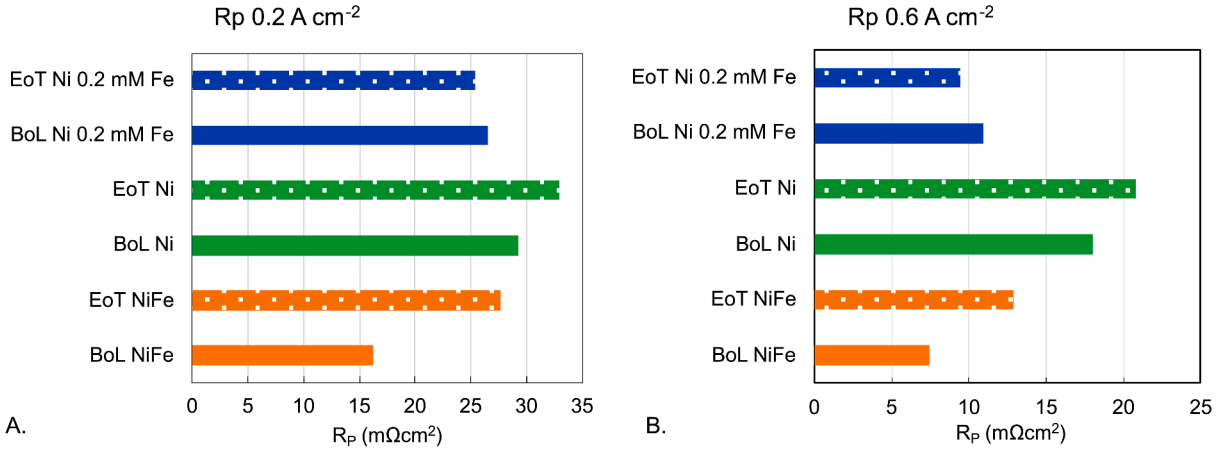

Fig. 7. Polarization resistances during BoL (fully colored) and EoT (dotted), obtained from EIS ECM fit, data recorded at 60 °C using 1 M KOH in a 5 cm^2 flowcell with Ni or NiFe sputtered anodes, with or without 0.2 mM Fe in the electrolyte, with Dioxide Materials™ cathode and an Aemion+ membrane. Polarization resistances at 0.2 A cm^{-2} (a) and 0.6 A cm^{-2} (b).

intermediate reaction species of the OER [47].

After the stability test, the polarization resistance increased for all samples except for Ni with 0.2 mM Fe. Based on our hypothesis there are still sufficient Fe sites for the reaction at the EoT for the NiFe sample, whereas the Ni sample is limited by the availability of Fe (this aligns with the more strongly visible upward curvature in the EoT Tafel plot). These results also show that the NiFe samples have lost Fe, while the ohmic resistance has decreased, leading to a seemingly stable durability test. This shows the importance of analyzing the ohmic resistance, polarization resistance, and polarization curves independently.

The results show that translating the findings of an RDE study into real-life conditions, including impurities and other relevant components, provides added information. Although in both setups the performance improved by adding Fe, there were clear differences. While the 3-electrode tests often focus on the voltage reached at 10 mA cm^{-2} for shorter time periods, longer term stability can be tested in a flowcell, which is much more relevant to industrial electrolyzers. We also learned that adding Fe to the electrolyte may be sufficient to temporarily enhance the performance of cost-effective Ni electrodes, compared to fabricating expensive catalyst layers that only last for a brief period in a real electrolyzer. This also stresses the importance of reporting accurate Fe concentrations in the electrolyte for AEMWEs and AWEs, including colloids, considering the significant change in durability it causes.

4. Conclusions

This study underscores the crucial role of Fe in enhancing both the stability and efficiency of Ni-based catalysts under industrially relevant conditions. NiFe catalysts demonstrate immediate and strong OER activity in RDE setups, whereas sputtered Ni samples require cycling for activation, regardless of Fe concentration in the electrolyte. In-situ Raman spectroscopy revealed that NiOOH forms in the bulk when little or no Fe is present, but it was not detected at Fe contents above 23 wt %, indicating a bulk NiOOH structure may not be required to obtain good activity for Fe-containing the catalyst layers. It cannot be said with certainty that there was no NiOOH present outside the 12–14 nm probing depth.

In flowcell experiments, the performance of Ni, with and without spiked Fe, was superior in the first few hours of durability, though they both quickly lose performance: the Fe-free sample lost 200 mV performance in just 18 h, and Ni with 0.2 mM Fe 50 mV in 60 h. While overall performance of NiFe layers appear stable over 100 h, this is maintained through a decrease in kinetic activity from loss of Fe alongside a reduced ohmic resistance, perhaps from membrane thinning. On the cathode (with 0.2 mM Fe) needle-like Fe deposits were identified employing SEM-EDX. Combined with the deposits in the reservoirs and the reduced Fe concentration in the electrolyte post-test, it shows that spiked Fe does

not remain dissolved in the solution throughout a test and that the improved performance is only temporary. Tafel analysis reveals that samples with pronounced upward deviation at high current densities are less stable and contain less Fe, while linear Tafel behavior correlates with better durability, suggesting dissolved Fe enhances initial activity but may limit performance at higher current densities and long-term operation.

In summary, our findings show the importance of Fe in improving the stability and efficiency of Ni electrodes in high current density applications and underscore the need for scale-up experiments in industry-relevant environments and contributes to the understanding of the role of Fe in the OER activity of Ni. Comparing RDE and flowcell results highlights the limitations of RDE testing for predicting real-world electrolyzer behavior as RDE setups fail to capture critical factors such as long-term stability, electrolyte impurities, MEA component interactions, and discrepancies in catalyst behavior.

CRediT authorship contribution statement

Ellis J. Donker: Writing – original draft, Visualization, Methodology, Investigation, Formal analysis, Data curation, Conceptualization. **Marcelle Potgieter:** Writing – review & editing, Supervision, Methodology, Data curation, Conceptualization. **Jordi Creus:** Funding acquisition, Conceptualization. **Marco B.S. Wonink:** Writing – review & editing, Supervision, Funding acquisition. **Matheus T. de Groot:** Writing – review & editing, Supervision, Investigation, Conceptualization. **Roelof J. Kriek:** Supervision, Project administration, Funding acquisition. **Frode Seland:** Supervision, Project administration, Funding acquisition. **Svein Sunde:** Supervision, Project administration, Funding acquisition.

Declaration of competing interest

The authors declare that they have no known competing financial interests or personal relationships that could have appeared to influence the work reported in this paper.

Acknowledgements

The RDE and Raman work was performed within the SANOCEAN project (South Africa/Norway Joint Research Programme on Ocean Research, including blue economy, climate change, the environment, and sustainable energy). The project is financially supported by the National Research Foundation of South Africa (NRF) and the Research Council of Norway (288590). This work is based on the research supported wholly/in part by the National Research Foundation of South Africa (Grant Numbers: 123025 and 118753).

This flowcell work receives a Dutch National Growth Fund contribution from the NXTGEN programme HIGH-TECH.

Supplementary materials

Supplementary material associated with this article can be found, in the online version, at doi:10.1016/j.electacta.2026.148639.

Data availability

Data will be made available on request.

References

[1] R. Kostecki, F. McLarnon, Electrochemical and In situ raman spectroscopic characterization of nickel hydroxide electrodes: i. Pure nickel hydroxide, J. Electrochem. Soc. 144 (2) (1997) 485, https://doi.org/10.1149/1.1837437.

[2] A. Faid, S. Sunde, Anion exchange membrane water electrolysis from catalyst design to the membrane electrode assembly, Energy Technol 10 (9) (2022), https://doi.org/10.1002/ente.202200506.

[3] W.U. Mulk, et al., Electrochemical hydrogen production through anion exchange membrane water electrolysis (AEMWE): recent progress and associated challenges in hydrogen production, Int. J. Hydrog. Energy 94 (2024) 1174–1211, https://doi.org/10.1016/j.ijhydene.2024.11.143.

[4] C. Santoro, et al., What is next in Anion-Exchange membrane water electrolyzers? Bottlenecks, benefits, and future, ChemSusChem. 15 (8) (2022) e202200027, https://doi.org/10.1002/cssc.202200027.

[5] S. Krishnan, et al., Present and future cost of alkaline and PEM electrolyser stacks, Int. J. Hydrog. Energy 48 (83) (2023) 83, https://doi.org/10.1016/j.ijhydene.2023.05.031. Art. no.

[6] R.-T. Liu, et al., Recent advances in proton exchange membrane water electrolysis, Chem. Soc. Rev. 52 (16) (2023) 5652–5683, https://doi.org/10.1039/D2CS00681B.

[7] L. Trotochaud, S.L. Young, J.K. Ranney, S.W. Boettcher, Nickel–Iron oxyhydroxide oxygen-evolution electrocatalysts: the role of intentional and incidental iron incorporation, J. Am. Chem. Soc. 136 (18) (2014) 6744–6753, https://doi.org/10.1021/ja502379c.

[8] D.A. Corrigan, The catalysis of the oxygen evolution reaction by iron impurities in thin film nickel oxide electrodes, J. Electrochem. Soc. 134 (2) (1987) 377, https://doi.org/10.1149/1.2100463.

[9] N. Chen, S.Y. Paek, J.Y. Lee, J.H. Park, S.Y. Lee, Y.M. Lee, High-performance anion exchange membrane water electrolyzers with a current density of 7.68 A cm−2 and a durability of 1000 h, Energy Environ. Sci. 14 (12) (2021) 6338–6348, https://doi.org/10.1039/D1EE02642A.

[10] B. Motealleh, Z. Liu, R.I. Masel, J.P. Sculley, Z.Richard Ni, L. Meroueh, Next-generation anion exchange membrane water electrolyzers operating for commercially relevant lifetimes, Int. J. Hydrog. Energy 46 (5) (2021) 3379–3386, https://doi.org/10.1016/j.ijhydene.2020.10.244.

[11] E. Cossar, A. Oyarce Barnett, F. Seland, and E.A. Baranova, "The performance of nickel and nickel-iron catalysts evaluated As anodes in anion exchange membrane water electrolysis," *Catalysts*, vol. 9, no. 10, Art. no. 10, 2019, doi: 10.3390/catal9100814.

[12] M. Busch, Water oxidation: from mechanisms to limitations, Curr. Opin. Electrochem. 9 (2018) 278–284, https://doi.org/10.1016/j.coelec.2018.06.007.

[13] M. Yu, E. Budiyanto, H. Tüysüz, Principles of water electrolysis and recent progress in cobalt-, nickel-, and iron-based oxides for the oxygen evolution reaction, Angew. Chem. Int. Ed. 61 (1) (2022) e202103824, https://doi.org/10.1002/anie.202103824.

[14] L. Bai, S. Lee, X. Hu, Spectroscopic and electrokinetic evidence for a bifunctional mechanism of the oxygen evolution reaction, Angew. Chem. Int. Ed. 60 (6) (2021) 3095–3103, https://doi.org/10.1002/anie.202011388.

[15] J. Rossmeisl, Z.-W. Qu, H. Zhu, G.-J. Kroes, J.K. Nørskov, Electrolysis of water on oxide surfaces, J. Electroanal. Chem. 607 (1) (2007) 83–89, https://doi.org/10.1016/j.jelechem.2006.11.008.

[16] S. Lee, K. Banjac, M. Lingenfelder, X. Hu, Oxygen isotope labeling experiments reveal different reaction sites for the Oxygen evolution reaction on nickel and nickel iron oxides, Angew. Chem. Int. Ed. 58 (30) (2019) 10295–10299, https://doi.org/10.1002/anie.201903200.

[17] F. Song, et al., Transition metal oxides as electrocatalysts for the oxygen evolution reaction in alkaline solutions: an application-inspired renaissance, J. Am. Chem. Soc. 140 (25) (2018) 7748–7759, https://doi.org/10.1021/jacs.8b04546.

[18] M. Busch, E. Ahlberg, I. Panas, Electrocatalytic oxygen evolution from water on a Mn(III–V) dimer model catalyst—a DFT perspective, Phys. Chem. Chem. Phys. 13 (33) (2011) 15069–15076, https://doi.org/10.1039/C0CP02132F.

[19] M. Busch, N.B. Halck, U.I. Kramm, S. Siahrostami, P. Krtil, J. Rossmeisl, Beyond the top of the volcano? – a unified approach to electrocatalytic oxygen reduction and oxygen evolution, Nano Energy 29 (2016) 126–135, https://doi.org/10.1016/j.nanoen.2016.04.011.

[20] M. Görlin, et al., Oxygen evolution reaction dynamics, faradaic charge efficiency, and the active metal redox states of Ni-Fe oxide water splitting electrocatalysts, J. Am. Chem. Soc. 138 (17) (2016) 5603–5614, https://doi.org/10.1021/jacs.6b00332.

[21] N.B. Halck, V. Petrykin, P. Krtil, J. Rossmeisl, Beyond the volcano limitations in electrocatalysis - oxygen evolution reaction, Phys. Chem. Chem. Phys. 16 (27) (2014) 13682–13688, https://doi.org/10.1039/c4cp00571f.

[22] M. Görlin, et al., Tracking catalyst redox states and reaction dynamics in Ni–Fe oxyhydroxide oxygen evolution reaction electrocatalysts: the role of catalyst support and electrolyte pH, J. Am. Chem. Soc. 139 (5) (2017) 2070–2082, https://doi.org/10.1021/jacs.6b12250.

[23] M. Burke Stevens, et al., Revised oxygen evolution reaction activity trends for first-row transition-metal (Oxy)hydroxides in alkaline media, J. Phys. Chem. Lett. 6 (18) (2015) 3737–3742, https://doi.org/10.1021/acs.jpclett.5b01650.

[24] L. Trotochaud, S.L. Young, J.K. Ranney, S.W. Boettcher, Nickel–Iron oxyhydroxide oxygen-evolution electrocatalysts: the role of intentional and incidental iron incorporation, J. Am. Chem. Soc. 136 (18) (2014) 18, https://doi.org/10.1021/ja502379c. Art. no.

[25] R. Farhat, J. Dhainy, L.I. Halaoui, OER catalysis at activated and codeposited NiFe-oxo/hydroxide thin films is due to postdeposition surface-Fe and is not sustainable without Fe in solution, ACS Catal 10 (1) (2020) 20–35, https://doi.org/10.1021/acscatal.9b02580.

[26] M.Burke Stevens, C.D.M. Trang, L.J. Enman, J. Deng, S.W. Boettcher, Reactive Fe-sites in Ni/Fe (Oxy)hydroxide are responsible for exceptional oxygen electrocatalysis activity, J. Am. Chem. Soc. 139 (33) (2017) 11361–11364, https://doi.org/10.1021/jacs.7b07117.

[27] D.Y. Chung, et al., Dynamic stability of active sites in hydr(oxy)oxides for the oxygen evolution reaction, Nat. Energy 5 (3) (2020) 3, https://doi.org/10.1038/s41560-020-0576-y. Art. no.

[28] M.M. Heath, M. Potgieter, F. Seland, S. Sunde, R.J. Kriek, Enhancing the oxygen evolution reaction activity of sputtered Ni, NiO, and NiNiO thin films by incorporating Fe, ChemElectroChem 11 (4) (2024) e202300485, https://doi.org/10.1002/celc.202300485.

[29] K.L. Nardi, N. Yang, C.F. Dickens, A.L. Strickler, S.F. Bent, Creating highly active atomic layer deposited NiO electrocatalysts for the oxygen evolution reaction, Adv. Energy Mater. 5 (17) (2015) 1500412, https://doi.org/10.1002/aenm.201500412.

[30] H. Bode, K. Dehmelt, J. Witte, Zur kenntnis der nickelhydroxidelektrode—i.Über das nickel (II)-hydroxidhydrat, Electrochim. Acta. 11 (8) (1966) 1079–1087, https://doi.org/10.1016/0013-4686(66)80045-2.

[31] D.S. Hall, D.J. Lockwood, C. Bock, B.R. MacDougall, Nickel hydroxides and related materials: a review of their structures, synthesis and properties, Proc. R. Soc. Math. Phys. Eng. Sci. 471 (2174) (2015) 20140792, https://doi.org/10.1098/rspa.2014.0792.

[32] S.L. Medway, C.A. Lucas, A. Kowal, R.J. Nichols, D. Johnson, In situ studies of the oxidation of nickel electrodes in alkaline solution, J. Electroanal. Chem. 587 (1) (2006) 172–181, https://doi.org/10.1016/j.jelechem.2005.11.013.

[33] A. Seghiouer, J. Chevalet, A. Barhoun, F. Lantelme, Electrochemical oxidation of nickel in alkaline solutions: a voltammetric study and modelling, J. Electroanal. Chem. 442 (1–2) (1998) 113–123, https://doi.org/10.1016/S0022-0728(97)00498-1.

[34] W. Visscher, E. Barendrecht, The anodic oxidation of nickel in alkaline solution, Electrochim. Acta. 25 (5) (1980) 651–655, https://doi.org/10.1016/0013-4686(80)87072-1.

[35] J.L. Weininger, M.W. Bréiter, Effect of crystal structure on the anodic oxidation of nickel, J. Electrochem. Soc. 110 (6) (1963), https://doi.org/10.1149/1.2425798.

[36] S. Mellsop, A. Gardiner, B. Johannessen, A. Marshall, Structure and transformation of oxy-hydroxide films on Ni anodes below and above the oxygen evolution potential in alkaline electrolytes, Electrochim. Acta. 168 (2015), https://doi.org/10.1016/j.electacta.2015.04.020.

[37] B.S. Yeo, A.T. Bell, In Situ Raman study of nickel oxide and gold-supported nickel oxide catalysts for the electrochemical evolution of oxygen, J. Phys. Chem. C 116 (15) (2012), https://doi.org/10.1021/jp3007415.

[38] S. Haghverdi Khamene, C. van Helvoirt, M.N. Tsampas, M. Creatore, Electrochemical activation of atomic-layer-deposited nickel oxide for water oxidation, J. Phys. Chem. C 127 (46) (2023) 22570–22582, https://doi.org/10.1021/acs.jpcc.3c05002.

[39] I.J. Godwin, M.E.G. Lyons, Enhanced oxygen evolution at hydrous nickel oxide electrodes via electrochemical ageing in alkaline solution, Electrochem. Commun. 32 (2013) 39–42, https://doi.org/10.1016/j.elecom.2013.03.040.

[40] Y.-F. Li, A. Selloni, Mechanism and activity of water oxidation on selected surfaces of pure and Fe-doped NiOx, ACS Catal 4 (4) (2014) 1148–1153, https://doi.org/10.1021/cs401245q.

[41] M.W. Louie, A.T. Bell, An investigation of thin-film Ni–Fe oxide catalysts for the electrochemical evolution of oxygen, J. Am. Chem. Soc. 135 (33) (2013) 12329–12337, https://doi.org/10.1021/ja405351s.

[42] M. Demnitz, Y. Martins Lamas, R. Lira Garcia Barros, A.W.N. de Leeuw den Bouter, J. van der Schaaf, M.T.(Thijs) De Groot, Effect of iron addition to the electrolyte on alkaline water electrolysis performance, IScience 27 (1) (2024) 108695, https://doi.org/10.1016/j.isci.2023.108695.

[43] M. Ranz, B. Grabner, B. Schweighofer, H. Wegleiter, A. Trattner, Dynamics of anion exchange membrane electrolysis: unravelling loss mechanisms with electrochemical impedance spectroscopy, reference electrodes and distribution of relaxation times, J. Power Source. 605 (234455) (2024), https://doi.org/10.1016/j.jpowsour.2024.234455.

[44] A.Y. Faid, A.O. Barnett, F. Seland, S. Sunde, NiCu mixed metal oxide catalyst for alkaline hydrogen evolution in anion exchange membrane water electrolysis, Electrochim. Acta. 371 (2021) 137837, https://doi.org/10.1016/j.electacta.2021.137837.

[45] P. Johnson, R. Christy, Optical constants of transition metals: ti, V, Cr, Mn, Fe, Co, Ni, and Pd, Phys. Rev. B 9 (12) (1974) 5056–5070, https://doi.org/10.1103/PhysRevB.9.5056.

[46] R. Subbaraman, et al., Trends in activity for the water electrolyser reactions on 3d M(Ni,Co,Fe,Mn) hydr(oxy)oxide catalysts, Nat. Mater. 11 (6) (2012) 550–557, https://doi.org/10.1038/nmat3313.

[47] D. Friebel, et al., Identification of highly active Fe sites in (Ni,Fe)OOH for electrocatalytic water splitting, J. Am. Chem. Soc. 137 (3) (2015) 1305–1313, https://doi.org/10.1021/ja511559d.

[48] S. Klaus, Y. Cai, M.W. Louie, L. Trotochaud, A.T. Bell, Effects of Fe electrolyte impurities on Ni(OH)2/NiOOH structure and oxygen evolution activity, J. Phys. Chem. C 119 (13) (2015) 7243–7254, https://doi.org/10.1021/acs.jpcc.5b00105.

[49] M.S. Burke, M.G. Kast, L. Trotochaud, A.M. Smith, S.W. Boettcher, Cobalt–Iron (Oxy)hydroxide oxygen evolution electrocatalysts: the role of structure and composition on activity, stability, and mechanism, J. Am. Chem. Soc. 137 (10) (2015) 3638–3648, https://doi.org/10.1021/jacs.5b00281.

[50] F. Tuinstra, J.L. Koenig, Raman Spectrum of Graphite, J. Chem. Phys. 53 (3) (1970) 1126–1130, https://doi.org/10.1063/1.1674108.

[51] C. Johnston, P.R. Graves, In situ raman spectroscopy study of the nickel oxyhydroxide electrode (NOE) system, Appl. Spectrosc. 44 (1) (1990) 105–115, https://doi.org/10.1366/0003702904085769.

[52] B.C. Cornilsen, P.J. Karjala, P.L. Loyselle, Structural models for nickel electrode active mass, J. Power Source. 22 (3) (1988) 351–357, https://doi.org/10.1016/0378-7753(88)80029-6.

[53] M. Görlin, et al., Tracking catalyst redox states and reaction dynamics in Ni–Fe oxyhydroxide oxygen evolution reaction electrocatalysts: the role of catalyst support and electrolyte pH, J. Am. Chem. Soc. 139 (5) (2017) 2070–2082, https://doi.org/10.1021/jacs.6b12250.

[54] S. Dresp, et al., Molecular understanding of the impact of saline contaminants and alkaline pH on NiFe layered double hydroxide oxygen evolution catalysts, ACS Catal 11 (12) (2021) 6800–6809, https://doi.org/10.1021/acscatal.1c00773.

[55] S. Mitrović, I. Perović, S. Brković, M. Seović, P. Laušević, I.A. Pašti, The electrolyte effects on the kinetics of hydrogen and oxygen evolution reaction on polycrystalline nickel in alkaline media, Int. J. Hydrog. Energy 177 (2025) 151605, https://doi.org/10.1016/j.ijhydene.2025.151605.

[56] D. Yan, M.Z. Bazant, P.M. Biesheuvel, M.C. Pugh, F.P. Dawson, Theory of linear sweep voltammetry with diffuse charge: unsupported electrolytes, thin films, and leaky membranes, Phys. Rev. E 95 (3) (2017) 033303, https://doi.org/10.1103/PhysRevE.95.033303.

[57] H. Yamada, K. Yoshii, M. Asahi, M. Chiku, Y. Kitazumi, Cyclic voltammetry part 1: fundamentals, Electrochemistry 90 (10) (2022) 102005, https://doi.org/10.5796/electrochemistry.22-66082.

[58] F. Hegge, et al., Efficient and stable low iridium loaded anodes for PEM water electrolysis made possible by nanofiber interlayers, ACS Appl. Energy Mater. 3 (9) (2020) 8276–8284, https://doi.org/10.1021/acsaem.0c00735.

[59] W. Stumm, G.F. Lee, Oxygenation of ferrous iron, Ind. Eng. Chem. 53 (2) (1961) 143–146, https://doi.org/10.1021/ie50614a030.

[60] M. Pourbaix, Atlas of Electrochemical Equilibria in Aqueous Solutions, Pergamon Press Ltd., Oxford, 1966.

[61] H.R. Zamanizadeh, A. Oyarce Barnett, S. Sunde, B.G. Pollet, F. Seland, Performance of activated stainless steel and nickel-based anodes in alkaline water electrolyser, J. Power Source. 564 (2023) 232828, https://doi.org/10.1016/j.jpowsour.2023.232828.

[62] S. Poli, et al., Regeneration of iron species for high and stable activity of nickel electrodes in the oxygen evolution reaction, Green Chem 27 (28) (2025) 8505–8516, https://doi.org/10.1039/D5GC00114E.

[63] N. Watson, M. Keegan, B. Bosch, N. Yan, G. Rothenberg, The influence of metal impurities on NiOOH electrocatalytic activity in the oxygen evolution reaction, ChemElectroChem 11 (2024), https://doi.org/10.1002/celc.202400223.

[64] O. van der Heijden, S. Park, R.E. Vos, J.J.J. Eggebeen, M.T.M. Koper, Tafel slope plot as a tool to analyze electrocatalytic reactions, ACS Energy Lett 9 (4) (2024) 1871–1879, https://doi.org/10.1021/acsenergylett.4c00266.

[65] R.A. Armstrong, G.W.D. Briggs, M.A. Moore, The effect of lithium in preventing iron poisoning in the nickel hydroxide electrode, Electrochim. Acta 31 (1) (1986) 25–27, https://doi.org/10.1016/0013-4686(86)80056-1.

[66] D.S. Cameron, R.L. Phillips, P.M. Willis, Poison tolerant platinum catalysed cathodes for membrane cells, in: N.M. Prout, J.S. Moorhouse (Eds.), Modern Chlor-Alkali Technology, Modern Chlor-Alkali Technology, 4, Springer Netherlands, Dordrecht, 1990, pp. 95–107, https://doi.org/10.1007/978-94-009-1137-6_10.

[67] L. Brossard, Electrocatalytic performance for alkaline water electrolysis of Ni electrodes electrocoated with Fe or Fe/Mo, Int. J. Hydrog. Energy 16 (1) (1991) 13–21, https://doi.org/10.1016/0360-3199(91)90056-O.

[68] S.H. Frensch, et al., Impact of iron and hydrogen peroxide on membrane degradation for polymer electrolyte membrane water electrolysis: computational and experimental investigation on fluoride emission, J. Power Sources 420 (2019) 54–62, https://doi.org/10.1016/j.jpowsour.2019.02.076.

[69] F. Fouda-Onana, M. Chandesris, V. Médeau, S. Chelghoum, D. Thoby, N. Guillet, Investigation on the degradation of MEAs for PEM water electrolysers part I: effects of testing conditions on MEA performances and membrane properties, Int. J. Hydrog. Energy 41 (38) (2016) 16627–16636, https://doi.org/10.1016/j.ijhydene.2016.07.125.

[70] K.E. Ayers, et al., Characterization of anion exchange membrane technology for low cost electrolysis: symposium on Fuel Cell membranes, Electrode binders, and MEA Performance - 221st ECS meeting, Fuel Cell Membr. Electrode Bind. MEA Perform. 45 (23) (2012) 121–130, https://doi.org/10.1149/04523.0121ecst.

[71] L. Piccolo, Restructuring effects of the chemical environment in metal nanocatalysis and single-atom catalysis, Catal. Today 373 (2021) 80–97, https://doi.org/10.1016/j.cattod.2020.03.052.

[72] D.A. Harrington, P. van den Driessche, Mechanism and equivalent circuits in electrochemical impedance spectroscopy, Electrochim. Acta 56 (23) (2011) 8005–8013, https://doi.org/10.1016/j.electacta.2011.01.067.

[73] S. Anantharaj, S. Kundu, S. Noda, The Fe Effect': a review unveiling the critical roles of Fe in enhancing OER activity of Ni and Co based catalysts, Nano Energy 80 (2021) 105514, https://doi.org/10.1016/j.nanoen.2020.105514.

[74] Y. Rao, C. Cai, J. Tan, M. Pan, Oxygen reduction activity indicator for fuel cell catalysts at rated voltage, J. Electrochem. Soc. 166 (6) (2019) F351, https://doi.org/10.1149/2.0021906jes.

[75] P. Boillat, F.N. Büchi, L. Gubler, T.J. Schmidt, Use and misuse of electrochemical impedance spectroscopy (EIS) in fuel cell research, ECS Meet. Abstr. (32) (2019) 1435, https://doi.org/10.1149/MA2019-02/32/1435. MA2019-02.